The role of dissipation in the evolution of ocean swell

Diane M. Henderson[1] and Harvey Segur[2]

Received 22 March 2013; revised 21 June 2013; accepted 21 July 2013.

[1] Dissipation of ocean swell, inferred from published oceanographic data, is investigated to determine if laboratory results on the dissipative stabilization of narrow-banded wave trains are applicable to ocean swell. Three issues are addressed. (i) Dimensional decay rates of ocean swell are about a million times smaller than typical decay rates of laboratory waves. Nevertheless, when decay rates are nondimensionalized using scales of dispersive and nonlinear effects, the dimensionless decay rates of ocean swell are comparable to those of laboratory waves, indicating that dissipation and nonlinear effects can influence ocean swell on the same time scale. (ii) The stability of ocean swell to small perturbations is examined within the theoretical framework of nonlinear Schrödinger-type models that either do or do not include dissipation. As in laboratory experiments, for swell with small enough nonlinearity, dissipation can inhibit and eventually stop the growth of small perturbations before nonlinearity becomes important. And as in laboratory experiments, we document herein an example of ocean swell with stronger nonlinearity that exhibits frequency downshifting, which is not predicted by any nonlinear Schrödinger-type model, including higher-order models, with or without dissipation. (iii) Given that dissipation can influence the evolution of ocean swell, we compare the predicted decay rates of four (published) dissipative models with observed decay rates, both in the ocean and in a laboratory wave tank. The model that presupposes an inextensible film on the free surface agrees best with measured rates of dissipation of ocean swell.

Citation: Henderson, D. M., and H. Segur (2013), The role of dissipation in the evolution of ocean swell, *J. Geophys. Res. Oceans*, *118*, doi:10.1002/jgrc.20324.

1. Statement of the Problem

[2] Ocean "swell" refers to slowly varying wave trains of surface water waves, which are typically generated by an oceanic storm, and which are observed to propagate over thousands of km without additional forcing [*Snodgrass et al*., 1966]. The standard mathematical model of the dynamics of surface water waves, first posed by *Stokes* [1847], is an energy-conserving system, with no dissipation. But water and air are both viscous fluids, so the energy of ocean swell must dissipate as the swell propagates. The dissipation rate of ocean swell is measurable [cf. *Collard et al*., 2009] but weak enough that *Snodgrass et al*. [1966] pronounced it "negligible" in their landmark paper. It appears that they meant that dissipation is negligible in the sense that ocean swell can propagate the entire length of the Pacific Ocean, more than 1/3 of the distance around the world, while still maintaining measurable wave amplitudes and significant coherence.

[3] At about the same time as the important work of *Snodgrass et al*. [1966], several scientists around the world discovered what is now called either the "modulational instability" or the "Benjamin-Feir instability" [*Lighthill*, 1965; *Benjamin and Feir*, 1967; *Benney and Newell*, 1967; *Ostrovsky*, 1967; *Whitham*, 1967; *Zakharov*, 1967, 1968]. The instability occurs in energy-conserving systems with dispersive waves (i.e., in which waves with different frequencies travel at different speeds). A consequence of this instability is that in many physical situations, a uniform train of plane waves of finite but small amplitude is likely to be unstable. An approximate model that describes this process is the nonlinear Schrödinger (NLS) equation. In two spatial dimensions, this equation has the form

$$i\partial_\tau A + \alpha\partial_\xi^2 A + \beta\partial_\eta^2 A + \gamma|A|^2 A = 0, \qquad (1)$$

where $A(\xi, \eta, \tau)$ describes the complex, two-dimensional envelope of a train of nearly monochromatic, nearly plane waves, with the rapid oscillation of individual wave crests and troughs averaged out; ξ and η are slowly varying spatial variables, in a coordinate system moving with a representative group velocity of the waves; τ is an even more slowly varying time-like variable, to mark the slow evolution of the wave train, after both the rapid oscillations and

[1]Department of Mathematics, Penn State University, University Park, Pennsylvania, USA.
[2]Applied Mathematics Department, University of Colorado Boulder, Boulder, Colorado, USA.

Corresponding author: D. M. Henderson, Department of Mathematics, Penn State University, University Park, PA 16802, USA. (dmh@math.psu.edu)

2169-9275/13/10.1002/jgrc.20324

the effect of group velocity have been taken into account; and $\{\alpha, \beta, \gamma\}$ are real-valued constants, which are derived from the original problem. See *Sulem and Sulem* [1999] for a discussion of some of the many physical applications of this model.

[4] This instability is relevant to ocean swell because (1) describes approximately the inviscid dynamics of surface waves on deep water, as noted by *Zakharov* [1968]. For gravity-induced surface water waves without dissipation, $\alpha\gamma > 0$, $\alpha\beta \leq 0$ in (1). Then, it is straightforward to show that any spatially uniform solution of (1), which has $|A| = const.$ and which represents a uniform train of plane waves, is unstable. Because ocean swell is dispersive, it tends more and more toward a uniform train of gravity-induced plane waves on deep water, so swell is unstable according to (1). *Benjamin and Feir* [1967] emphasized that this instability leads to a spreading of wave energy in frequency-space and, therefore, to "the disintegration of wave trains on deep water." Later, other researchers proposed that the modulational instability might also lead to the formation of "freak waves" [*Calini and Schober*, 2002; *Janssen*, 2003; *Dyachenko and Zakharov*, 2005; *Onorato et al*., 2006; *Dysthe et al*., 2008]. The modulational instability has been a basic principle of nonlinear wave propagation ever since it was discovered.

[5] The work described herein was motivated in part by an interest in reconciling these two scientific developments: if ocean swell is unstable, as predicted by (1), how can it propagate coherently over thousands of kilometers, as documented by *Snodgrass et al*. [1966], *Collard et al*. [2009], and others? It is unclear (to us) how to reconcile this picture of energetic ocean swell that remains coherent over long distances with "the disintegration of wave trains on deep water," envisioned by *Benjamin and Feir* [1967].

[6] A possible resolution of this paradox was suggested by results of *Segur et al*. [2005], who found that adding even a small amount of dissipation to (1) can stabilize the modulational instability. Specifically, they showed that if (1) is generalized to

$$i\partial_\tau A + \alpha\partial_\xi^2 A + \beta\partial_\eta^2 A + \gamma|A|^2 A + i\delta A = 0, \tag{2}$$

where $\delta > 0$ represents dissipation in the system, then a spatially uniform wave train (with $|A| = \text{constant}$) can be *unstable* according to (1) with $\delta = 0$, but *stable* according to (2) for any $\delta > 0$ and for any real-valued choices of $\{\alpha, \beta, \gamma\}$. They provided experimental confirmation of their mathematical result, but dissipation rates in their experiments were much larger than those of ocean swell, so questions arose as to how well their laboratory experiments modeled the dynamics of ocean swell.

[7] The objective of this paper is to provide some of the basic information needed to create dissipative generalizations of (1) that are appropriate for ocean swell. Several issues need to be addressed.

[8] (a) What dissipation rates for swell are observed in the open ocean? Waves in a laboratory tank necessarily have much shorter wavelengths than those of ocean swell. When the dissipation rates of ocean waves and laboratory waves are each scaled properly, how do their respective values of the dimensionless (δ), used in (2), compare?

[9] (b) In order to replace the standard (nondissipative) model of surface water waves with a more accurate dissipative model, one can consider the water to be viscous and the fluid motion to be (weakly) rotational. In addition, one should reconsider the boundary conditions at the free surface, for two sets of reasons.

[10] 1. *Hunt* [1964], *Van Dorn* [1966], and others noted that the dissipation rates they observed in laboratory experiments on surface water waves were too large to be attributed solely to boundary layers on the sidewalls and bottoms of their wave tanks. *Van Dorn* [1966] hypothesized an additional boundary layer at the free surface to account for the extra dissipation observed.

[11] 2. *Van Dorn* [1966] also noted that dissipation rates in his laboratory experiments changed over time, and hypothesized that a contaminating film, growing on the free surface, might explain both the extra dissipation and its time-dependent nature. Similarly, *Segur et al*. [2005] found that measured dissipation rates in their wave tank increased slowly (over a period of hours to days). In addition, they found that an increased dissipation rate could be reduced nearly to its original value by skimming off a thin layer of water at the free surface. This observation is consistent with Van Dorn's hypothesis that a contaminating film grows slowly on the free surface. Whether there is an analogous dissipative effect due to film dynamics on the sea surface is unknown.

[12] The outline of this paper is as follows. In section 2, we use published oceanographic data [*Snodgrass et al*., 1966; *Collard et al*., 2009] to document observed dissipation rates in the open ocean. These observed rates show some scatter, but they all lie within a factor of two of each other. Oceanic dissipation rates are vastly smaller than dissipation rates observed in wave-tank experiments. Even so, when each dimensional dissipation rate is scaled appropriately to translate it into δ, the dimensionless dissipation parameter in (2), some values of δ for ocean swell and for waves in our tank are reasonably close. In section 3, we apply the model in (2) to swell events documented by *Snodgrass et al*. [1966] and *Collard et al*. [2009]. Their papers do not provide enough information about the observed swell to draw precise conclusions, but we can estimate how much sidebands might have grown for specific sets of observed ocean swell. Section 3 also contains a detailed discussion of frequency downshifting, which occurs outside the range of validity of either (1) or (2). In section 4, we analyze four dissipative models of surface water waves that have been proposed in the literature, to determine which of these models have (linearized) dissipation rates consistent with those observed both in laboratory experiments and in ocean swell.

[13] The main conclusion of this paper is that viscous dissipation, which usually has only a weak effect on the propagation of surface water waves forced by gravity, can affect the stability of those waves. Specifically, we find the following results.

[14] 1. The rate of viscous dissipation for ocean swell is vastly smaller than the rate of dissipation of surface waves in a laboratory wave tank. But ocean swell is also much less nonlinear than typical waves in a wave tank. The relative strength of dissipation versus nonlinearity is encoded in the dimensionless parameter δ in (2). The range of values

of δ for typical ocean swell overlaps the range of values for laboratory waves.

[15] 2. For ocean swell with small enough nonlinearity, dissipation impedes and can stop the modulational instability before sidebands grow appreciably.

[16] 3. For waves with strong enough nonlinearity, either in the carrier wave train (measured by ε) or in the initial size of the sidebands, the wave train can exhibit frequency downshifting, which is not predicted by either (1) or (2). We show in section 2 the first example known to us of frequency downshifting of freely propagating ocean waves.

[17] 4. Among the theoretical models mentioned above, the inextensible-film model provides the most accurate prediction of dissipation rates of ocean swell.

[18] A preliminary version of this paper was given by *Henderson and Segur* [2012].

2. Observed Dissipation Rates of Ocean Swell and of Laboratory Wave Trains

[19] In their classic paper, *Snodgrass et al*. [1966] set up a chain of up to six measuring stations along a great-circle path between New Zealand and Alaska, to record the propagation of ocean swell across the Pacific Ocean. Over 2.5 months, the authors tracked the swell from 12 different storms in the southern oceans. Ocean swell is dispersive, so the swell from a particular storm in the southern oceans might have passed the measuring station in New Zealand over about a day or less, but the same set of swell was spread over 5–6 days by the time it reached Alaska. Consequently, the wave spectra that the authors measured were often somewhat narrow-banded at the first measuring station, and they became even more narrow-banded at subsequent measuring stations, because the swell had more time to disperse.

[20] *Snodgrass et al*. [1966] processed their data to remove various undesired effects. They specifically mention adjusting their data to remove wave attenuation due to: (i) geometric spreading (on a two-dimensional spherical surface), (ii) island shadowing (i.e., blocking of swell by islands in the path), and (iii) refraction due to local variations in bathymetry. In addition, they filtered out the waves of the background sea state that coexisted with the swell. Herein, we use their processed data to deduce a measured rate of wave attenuation due to dissipation, for the swell from a specific storm.

[21] Figure 1 is Figure 20 from *Snodgrass et al*. [1966]. It shows measured spectra, $L(f)$, from a storm that occurred on August 1.9, as the swell passed Tutuila (in American Samoa, 14°20′S, 170°40′W), then Palmyra (5°50′N, 162°W), Honolulu (Hawaii, 21°10′N, 157°50′W), and finally Yakutat (Alaska, 59°30′ N, 140°20′W). These spectra are from 3 h time series taken at roughly 12 h intervals. One sees that (i) the peak frequency increases with time as the slower, higher frequency waves arrive at a given station and (ii) the spectra at a given frequency become more narrow-banded with increasing distance from the storm center. Figure 2 shows our digitization of three of the curves at a particular peak frequency (~52 mc/s), indicated by the arrows in Figure 1. Also in Figure 2 are conversions of these data to units of energy density, using

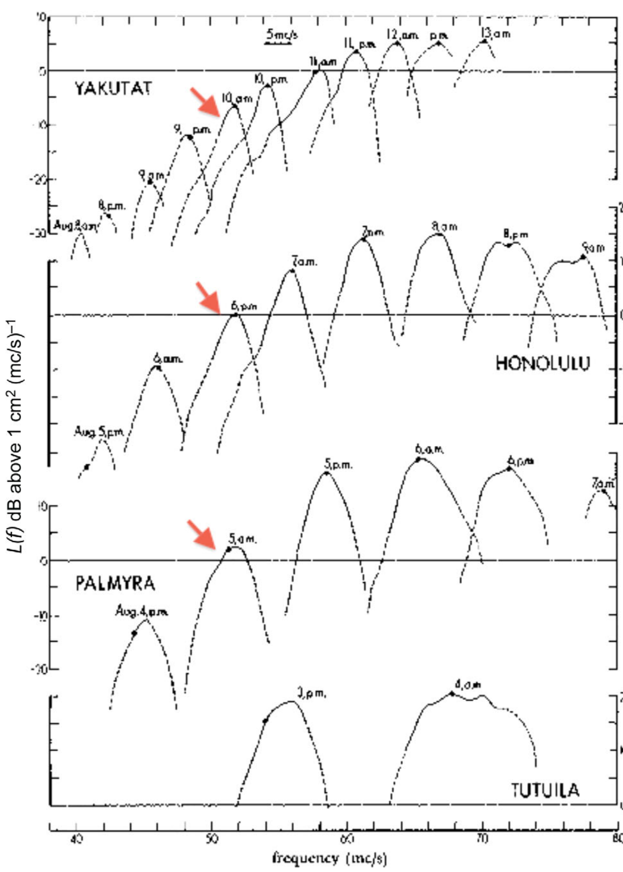

Figure 1. Spectral information from 3 h measurements of swell taken about every 12 h at the locations indicated (1 mc/s = 0.001 Hz) [*Snodgrass et al*., 1966, Figure 20]. The arrows indicate curves that are digitized and shown in Figure 2.

$\Phi(f) = 10^{L(f)/10}$. The exponentiated views show the narrow-bandedness of the 3 h spectra.

[22] A composite of these 3 h spectra provide a wave spectrum for the entire swell system from a given storm event. Figure 3a, a digitization of part of Figure 21 of *Snodgrass et al*. [1966], shows the measured composite spectra, $L(f)$, of the entire swell system from a storm that occurred on August 1.9. These composite spectra do not appear narrow-banded, because they contain the energy at each frequency over a period of several days. We use the composite spectra to compute total energy in the swell system and deduce an energy-decay rate. Again we converted these data to have units of energy density, using $\Phi(f) = 10^{L(f)/10}$. The resulting spectra are shown in Figure 3b. The area under each curve in Figure 3b provides a measure of the total energy in the swell system, denoted by M, at each gage site. For consistency, we integrate all four curves over the frequency interval available at Yakutat (the smallest interval). Figure 3c shows the change in total energy measured at successive locations, and the slope of the straight-line fit gives the energy-decay rate for this set of swell. Approximate distances between these locations are Tutuila-Palmyra: 2400 km; Palmyra-Honolulu: 1800 km; and Honolulu-Yakutat: 4500 km.

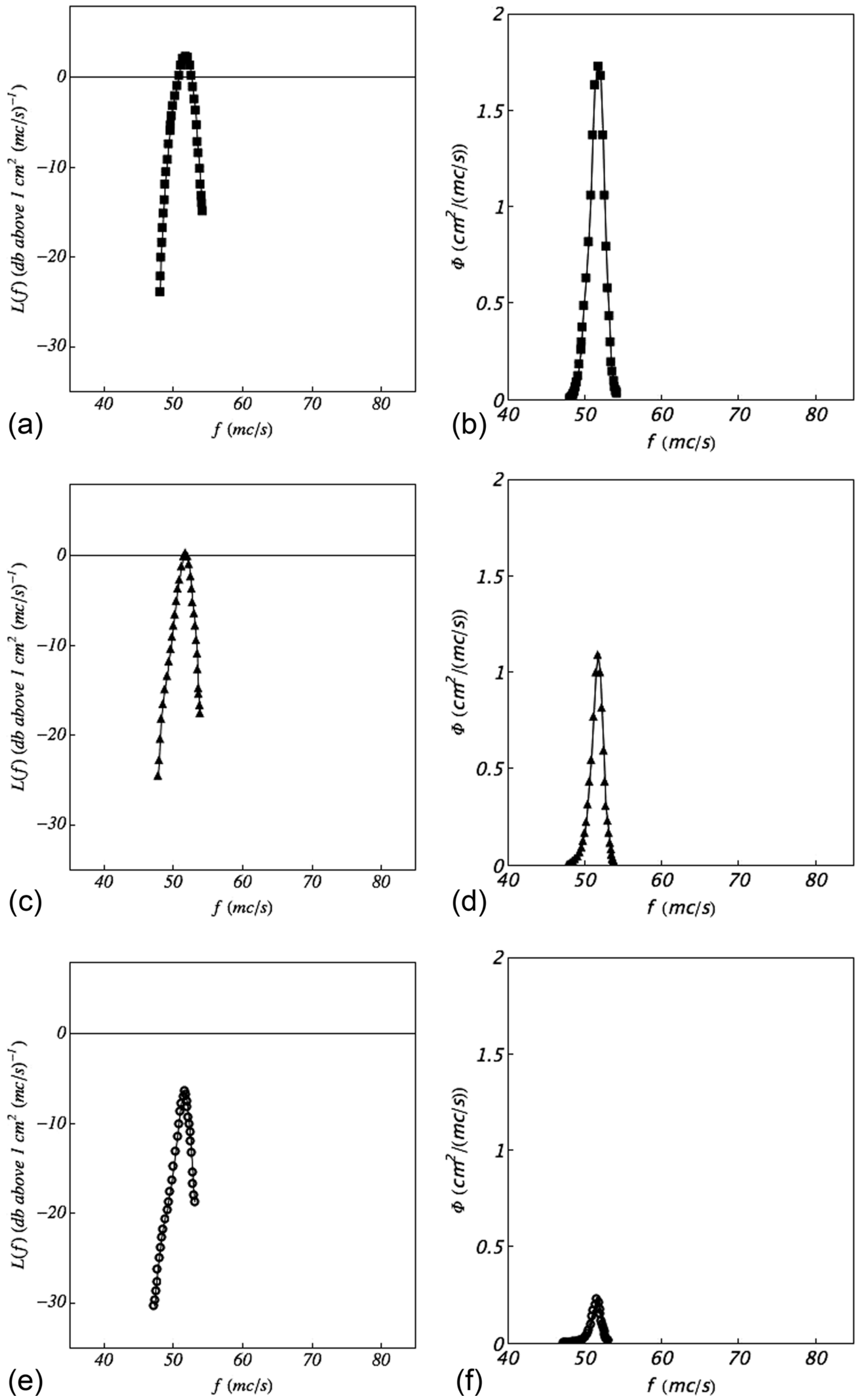

Figure 2. (a, c, and e) Digitized versions of the curves indicated by the arrows in Figure 1. (b, d, and f) Same information recomputed in units of energy density as a function of frequency using $\Phi(f) = 10^{L(f)/10}$, where f is frequency. (a and b) Palmyra (5 A.M.); (c and d) Honolulu (6 P.M.); and (e and f) Yakutat (10 A.M.).

[23] Figure 4 shows similar spectral information obtained from measurements of swell resulting from the August 13.7 storm, which were obtained at Cape Palliser (41°37′S, 175°20′W), Tutuila, Palmyra, Honolulu, and Yakutat. The spectrum obtained at Cape Palliser has two peaks, as shown in Figure 4b, indicating that dispersion had not yet separated the different frequency components. Since the spectrum obtained at this first site does not fit the

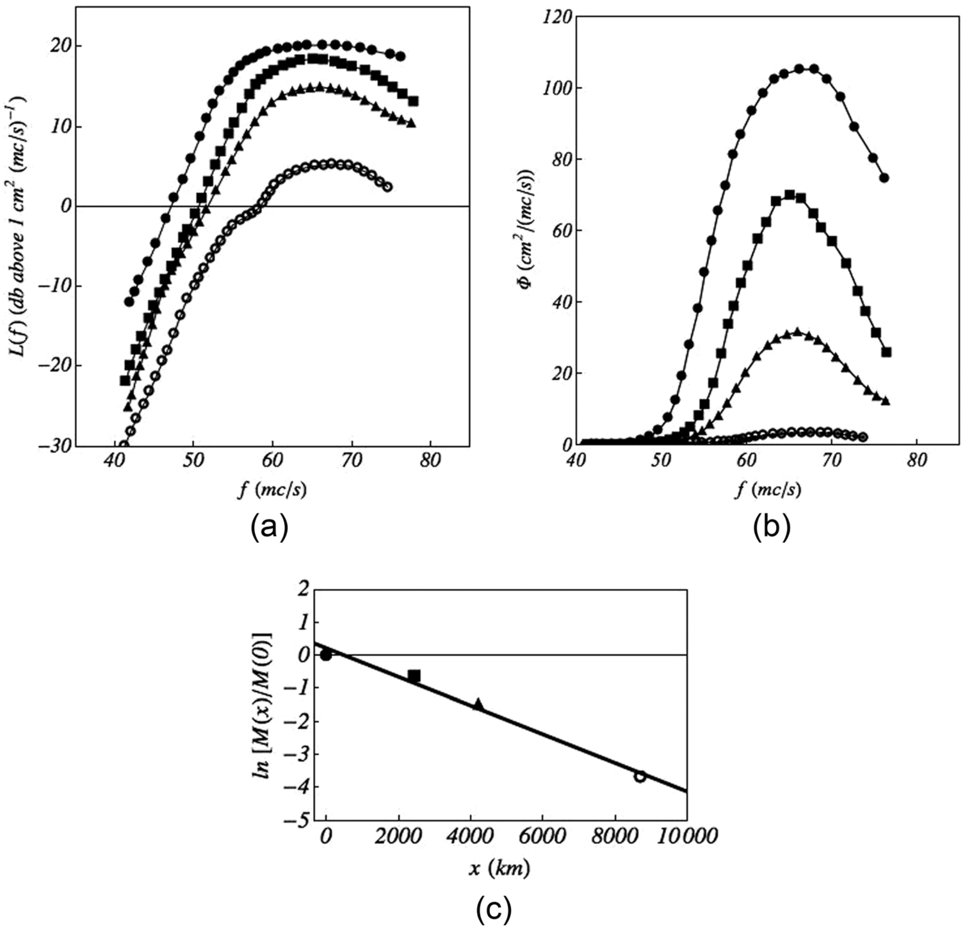

Figure 3. Spectral information from measurements of swell from the August 1.9 event of *Snodgrass et al*. [1966]. Symbols indicate data obtained at Tutuila (solid circles), Palmyra (squares), Honolulu (triangles), and Yakutat (hollow circles). (a) Digitized version of top part of Figure 21 in *Snodgrass et al*. [1966], with 1 mc/s = 0.001 Hz. (b) Same information recomputed in units of energy density as a function of frequency using $\Phi(f) = 10^{L(f)/10}$, where f is frequency. (c) Each datum point in Figure 3c corresponds to (the log of) the integral (using $41.2 < f < 74.6$ mc/s) of each Φ-curve in Figure 3b, giving the total energy, $M(x)$, in the swell at that location. The slope of the solid line gives the energy-decay rate, $\Delta = 0.43 \times 10^{-3}$ km^{-1}.

description of a narrow-banded wave train, we use the second data set, obtained at Tutuila, to determine initial amplitudes. Figure 4c is the same as Figure 4b, rescaled and without the curve from Cape Palliser. This closer look shows that the spectral peak shifts downward, from about 65 mc/s at Tutuila to 61 mc/s at Palmyra, then it remains at this lower frequency as the swell continues its propagation to Yakutat. We return to this process, called *frequency downshifting*, in section 3.

[24] Figure 5 shows similar spectral information for the July 23.2 storm, based on data measured at Tutuila, Palmyra, Honolulu, and Yakutat. Note that the wave energy recorded at Honolulu (triangles) is *bigger* than that at Palmyra (squares). This feature is clearly evident in the data of *Snodgrass et al*. [1966], but they do not comment on it. We consider it part of the scatter in their data.

[25] Table 1 summarizes the results from these three data sets. For each data set, it provides Δ, the measured energy-decay rate, ω_0, the most energetic frequency and a characteristic initial amplitude, $2|A_0| = \sqrt{2M_0}$, where M_0 is the total energy at Tutuila in each set of swell. The crest-to-trough wave height is twice this: $4\ |A_0|$.

[26] More recently, *Collard et al*. [2009] analyzed satellite synthetic aperture radar (SAR) observations of ocean waves to determine wave-attenuation rates for ocean swell that had propagated at least 4000 km from the specific storm on which they focused. These authors had abundant data from which to choose, so they were able to avoid effects like island shadowing, for which *Snodgrass et al*. [1966] had to correct their data. Eventually, the authors chose 35 sets of ocean swell from this storm, in which each set of swell had a spectrum with a central peak period of 15 s (so $\omega_0 = 0.42$ rad/s). After removing the effect of geometric spreading from their data, they computed an energy-decay rate that gave the best least-squares fit for all of their data:

$$\Delta = 0.37 \times 10^{-6} \mathrm{m}^{-1}. \tag{3a}$$

[27] In addition, they estimated that 1 standard deviation from this mean rate of energy-decay lay in a range:

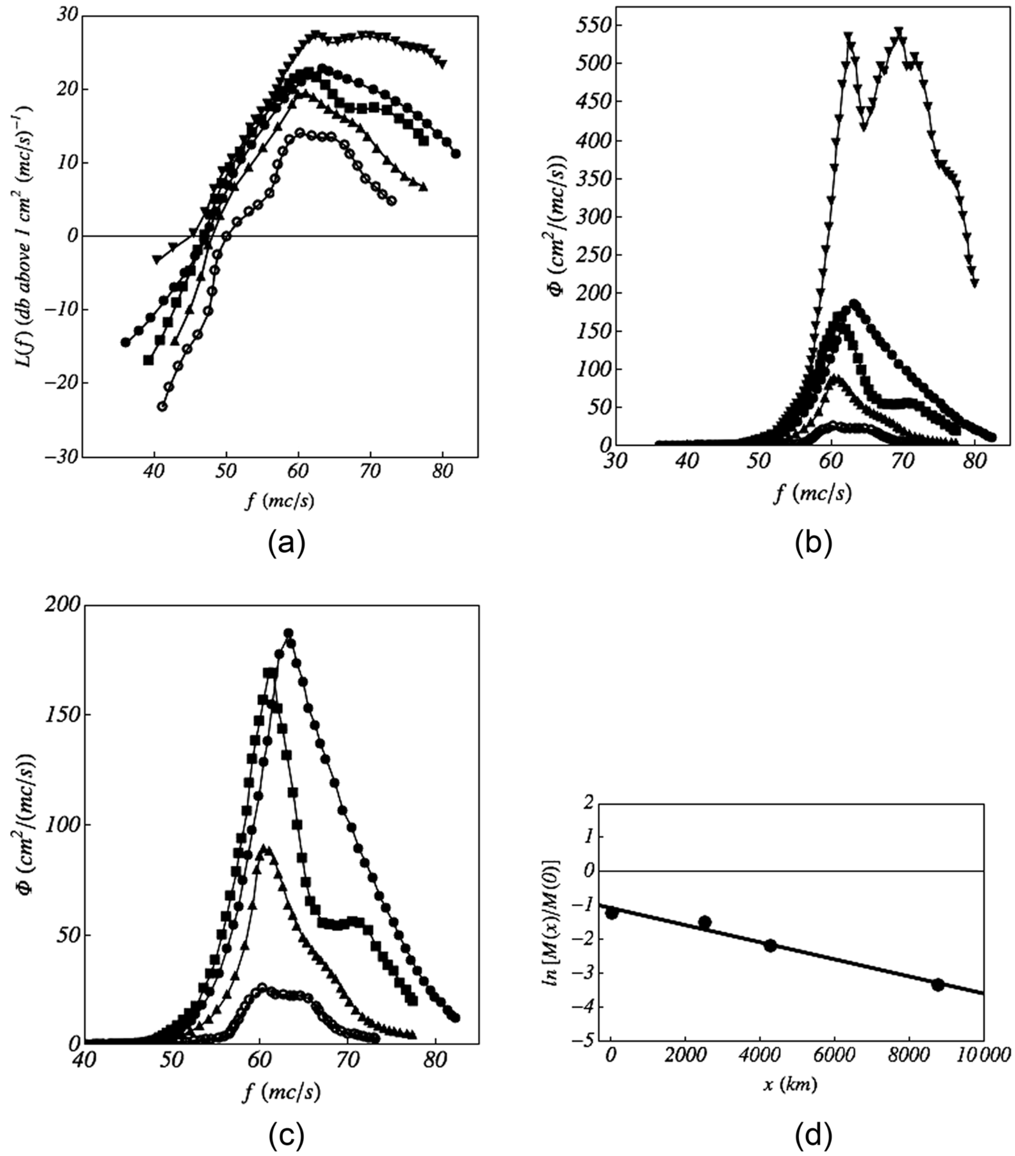

Figure 4. Spectral information from measurements of swell from the August 13.7 event from *Snodgrass et al*. [1966]. Symbols indicate data obtained at Cape Palliser (upside down triangle), Tutuila (solid circles), Palmyra (squares), Honolulu (triangles), and Yakutat (hollow circles). (a) Digitized version of top part of Figure 30 in *Snodgrass et al*. [1966]. (b) Same information recomputed in units of energy density. (c) Same information as in Figure 4b scaled to zoom in on the last four measurement sites. (d) Each datum point in Figure 4d corresponds to (the log of) the integral (using $41.2 < f < 73.4$ mc/s) of each Φ-curve in Figure 4c, giving the total energy, $M(x)$, in the swell at that location. The slope of the solid line gives the energy-decay rate, $\Delta = 0.25 \times 10^{-3}\ \mathrm{km}^{-1}$.

$$0.31 \times 10^{-6} < \Delta < 0.40 \times 10^{-6}\mathrm{m}^{-1}. \tag{3b}$$

[28] Our results, in Table 1, lie somewhat outside the range in (3b), but they are close enough that we can attribute the discrepancy to scatter in the data of *Snodgrass et al*. [1966].

[29] *Collard et al*. [2009] also gave an average significant swell height of 4.4 m for their data set, which leads to an r.m.s. value [*Dean and Dalrymple*, 1991] for the wave amplitude of:

$$2|A_0| = \frac{1}{2}\left(\frac{4.4}{1.4}\right) = 1.6\mathrm{m}. \tag{4}$$

Note that this wave amplitude is larger than any of those in Table 1, which are based on data of *Snodgrass et al*. [1966]. *Collard et al*. [2009] gave three reasons for this difference: (1) they intentionally chose a very energetic storm, to obtain good signal-to-noise ratios in their data; (2) their SAR data allowed them to follow the most energetic swell from the storm, while *Snodgrass et al*. [1966] could only measure waves along their fixed great-circle path; and (3) their filtered sample of 35 sets of swell contained no swell with small amplitudes, again to obtain good signal-to-noise ratios. We also note that the standard deviation of *Collard et al*. [2009], quoted in (3b), is based on the

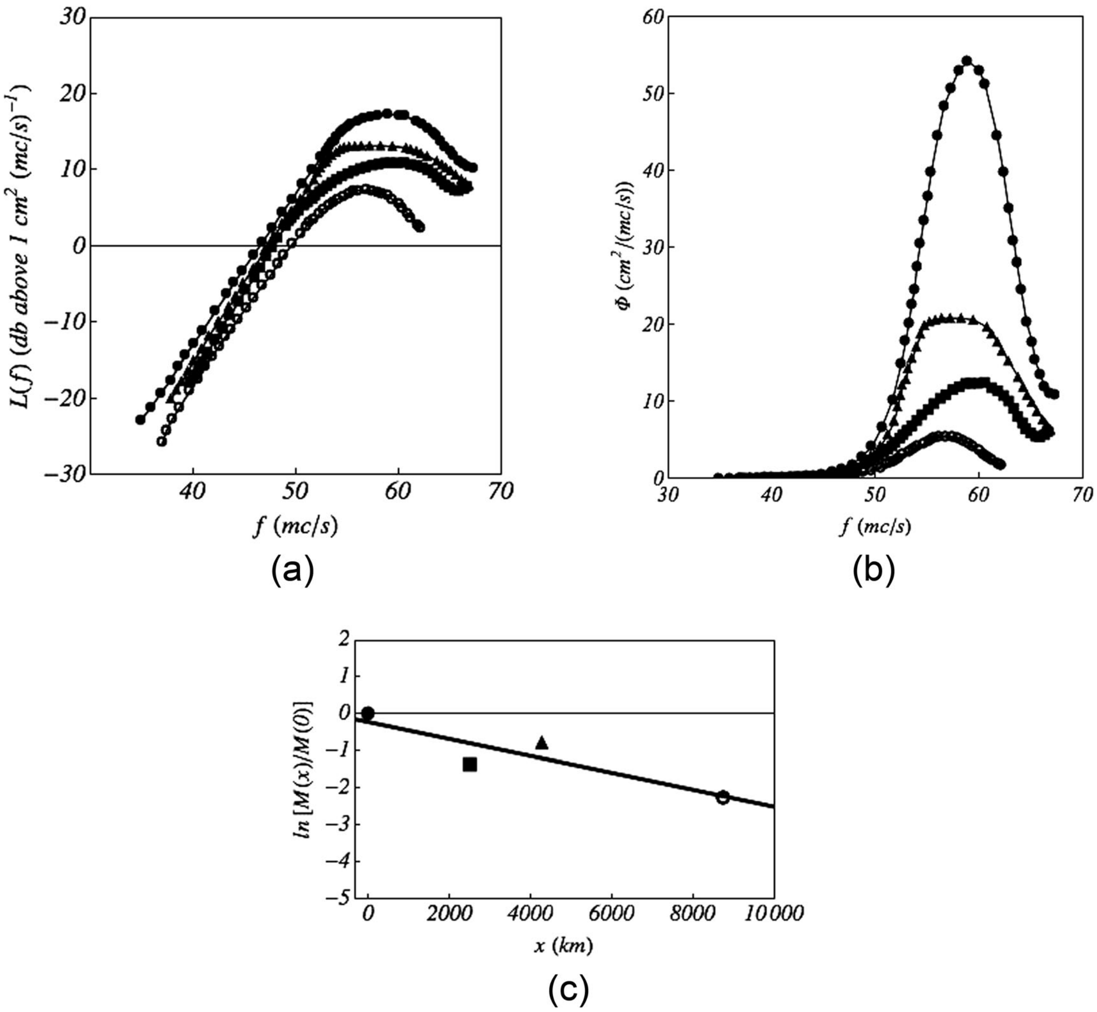

Figure 5. Spectral information from measurements of swell from the July 23.2 event from *Snodgrass et al*. [1966]. Symbols indicate data obtained at Tutuila (solid circles), Palmyra (squares), Honolulu (triangles), and Yakutat (hollow circles). (a) Digitized version of top part of Figure 26 (from about $30 < f < 65$ mc/s) in *Snodgrass et al*. [1966]. (b) Same information recomputed in units of energy density. (c) Each datum point in Figure 5c corresponds to (the log of) the integral (using $37.0 < f < 62.1$ mc/s) of each Φ-curve in Figure 5b, giving the total energy, $M(x)$, in the swell at that site. The slope of the solid line gives the energy-decay rate, $\Delta = 0.23 \times 10^{-3}\ \mathrm{km}^{-1}$.

swell generated by the single storm they studied. It need not apply to ocean swell in general.

[30] How do these observed decay rates for ocean swell, from either *Snodgrass et al*. [1966] or *Collard et al*. [2009], compare with decay rates of freely propagating waves in a laboratory wave tank? As mentioned above, *Segur et al*. [2005] found that the decay rate measured in their wave tank could depend on how long the water had been sitting in the tank since the water surface was last cleaned. They found that once the free surface of the water was cleaned, then the observed decay rate remained fairly constant for a period of a few hours—long enough to run a series of experiments. In this "cleaned surface" situation, they measured an amplitude-decay rate of 0.11 m^{-1} for waves on deep water. The wave energy is proportional to (amplitude)^2, so their observed energy-decay rate was twice this:

$$\Delta = 0.22\,\mathrm{m}^{-1}. \tag{5}$$

Thus, the observed energy-decay rate in this laboratory experiment was approximately a million times larger than that for ocean swell, as shown either in (3) or in Table 1, even though all of these waves are on deep water!

[31] However, this comparison might not be the most important one to make. Recall that (1) is designed to describe the evolution of a wave train due to nonlinear wave

Table 1. Summary of Three Systems Documented by *Snodgrass et al*. [1966][a]

Storm Date	Δ (m^{-1})	ω_0 (rad/s)	$2\lvert A_0\rvert$ (m)
Jul 23.2	0.23×10^{-6}	0.37	0.33
Aug 1.9	0.43×10^{-6}	0.41	0.64
Aug 13.7	0.25×10^{-6}	0.40	0.71

[a]Summary of results for the swell generated by storms on July 23.2, August 1.9, and August 13.7, as documented by *Snodgrass et al*. [1966]. For each storm, the table lists energy-decay rates (Δ), found in Figures 3c, 4d, and 5c, plus the peak frequencies (ω_0) and the characteristic initial amplitudes ($2|A_0|$), both recorded at the Tutuila site.

Table 2. Comparison of Dimensionless Dissipation Rates for Laboratory and Field Data[a]

Event	k_0 (m^{-1})	ε	Δ (m^{-1})	δ
Lab data [*Segur*, 2005]	44.1	0.10	0.22	0.25
Jul 23.2 [*Snodgrass*, 1966]	0.014	0.0046	0.23×10^{-6}	0.39
Aug 1.9 [*Snodgrass*, 1966]	0.017	0.011	0.43×10^{-6}	0.105
Aug13.7 [*Snodgrass*, 1966]	0.016	0.011	0.25×10^{-6}	0.065
Collard et al. [2009]	0.018	0.029	0.37×10^{-6}	0.012

[a]Wave numbers, measures of nonlinearity, measured energy-decay rates, and ratios of measures of dissipation to nonlinearity for a laboratory experiment and four oceanographic observations.

interactions and linear dispersion. The dimensionless parameter, δ, in (2), compares the distance scale for dissipation to distance scales for nonlinear interactions and dispersion. Δ is the (dimensional) distance scale for dissipation, either in a wave tank or in the ocean, so δ gives the ratio of Δ to the distance scale for nonlinear interactions (or for dispersion).

[32] The time-like variable (τ) in (1) or (2) actually measures how far the wave has traveled from its source; call this physical distance X. In (1) or (2), τ is a dimensionless, slow "time":

$$\tau = \varepsilon^2 k_0 X, \tag{6a}$$

where k_0 is the (dimensional) wave number of the carrier wave, and

$$\varepsilon = 2|A_0|k_0 \tag{6b}$$

is a dimensionless measure of the nonlinearity of the carrier wave [*Segur et al*., 2005]. In addition, there is an extra factor of 2 between Δ, an energy-decay rate, and δ, an amplitude-decay rate. It follows that the dimensionless δ is given by

$$\delta = \frac{\Delta}{2\varepsilon^2 k_0}. \tag{7}$$

[33] Now we can compute dimensionless values of δ, for the laboratory experiments of *Segur et al*. [2005], for ocean swell observed by *Snodgrass et al*. [1966] and for swell data of *Collard et al*. [2009]. We begin with the laboratory data. In addition to the energy-decay rate in (5), *Segur et al*. [2005] also measured other relevant parameters for their main set of experiments:

$$k_0 = 0.441\,\mathrm{cm}^{-1},\ \ 2|A_0| = 0.218\,\mathrm{cm} \;=>\; \varepsilon = 0.10. \tag{8}$$

[34] Equations (5), (7), and (8) yield the first line of Table 2. The information from Table 1, plus ($\omega_0{}^2 = gk_0$), the dispersion relation for gravity-induced waves on deep water, and (7) yield the next three lines of Table 2. Finally, using $\omega_0 = 0.42$, ($\omega_0{}^2 = gk_0$), (3a), (4) and (7) yield the last line of Table 2.

[35] Comments on Table 2:

[36] 1. Consider first only the ocean data, ignoring the first line in Table 2. Values of δ vary from each other by a factor of more than 30, even though the corresponding values of Δ vary by less than a factor of 2. This change is primarily due to the presence of ε, the nonlinearity parameter, defined by (6b). δ is a ratio that compares two distance scales, one representing dissipation and the other representing nonlinear interactions. Smaller values of ε (as for the July 23.2 storm) imply weaker nonlinear effects, so dissipation has more time to influence the dynamics of the waves.

[37] 2. A central question addressed in this paper is whether the wave damping that occurs naturally in the open ocean can stabilize the modulational instability for ocean swell. In the main set of lab experiments of *Segur et al*. [2005], dissipation in the wave tank stopped the modulational instability after some early growth of sidebands, as (2) predicts. The value of δ for the July 23.2 storm is larger than that for the lab experiment, while the values for the August 1.9 and August 13.7 storms are smaller by no more than a factor of 4, so one could conjecture that dissipation might have limited the growth of sidebands for the swell from these three storms as well. In section 3, we use (2) with appropriate values of δ to simulate how much sidebands might have grown for each of the three events documented by *Snodgrass et al*. [1966].

[38] 3. What happens if δ is quite small, as it is in the last row of Table 2? By the argument above, small δ means that the distance scale for dissipative effects is much longer than the distance scale for nonlinear interactions. Then (2) suggests that nonlinear effects, which drive the modulational instability, could make perturbations grow significantly before dissipation stops further growth. But laboratory experiments indicate instead that both (1) and (2) fail as valid models in this situation, because physical water waves exhibit frequency downshifting, which is not predicted by either (1) or (2). See section 3 for further discussion of downshifting.

3. Growth of Sidebands of Ocean Swell and the Effects of Dissipation

[39] In this section, we investigate the effects of measured dissipation rates, discussed in section 2, on the stability of sets of ocean swell propagating in one horizontal dimension. For this purpose, we recast (2) in dimensional form:

$$i\left(\partial_X A + \frac{\Delta}{2}A\right) + \alpha\partial_T^2 A + \gamma|A|^2 A = 0, \tag{9}$$

where the (dimensional) variables (X, T) are related to laboratory coordinates, (x, t), such that $X = \varepsilon^2 x$ is a slow space variable; $T = \varepsilon\left(t - x/C_g\right)$ is a slow time variable in a reference frame traveling at the carrier wave's group speed, C_g; $\varepsilon << 1$ is given in (6b); the dimensional coefficients, $\alpha = -k_0/\omega_0^2$ and $\gamma = -4k_0^3$, are consistent with the nondimensional values given in *Ablowitz and Segur* [1981]; $\{k_0, \omega_0(k_0)\}$are the wave number and corresponding frequency of the carrier wave; $A(X, T)$ is the slowly varying complex carrier-wave amplitude; and $\Delta/2$ is the amplitude-decay rate, listed in Table 2 for the events considered here. Following *Segur et al*. [2005], we consider a perturbed, Stokes-like solution to (9) of the form

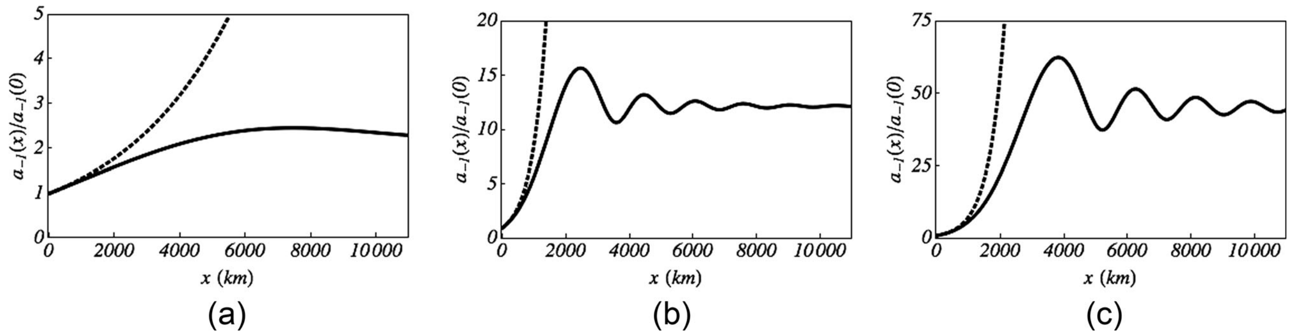

Figure 6. Evolution of sideband amplitudes from computations of (11). Solid curves have $\Delta > 0$ (with values listed in Table 2); dashed curves have $\Delta = 0$. (a) July 23.2 swell event, b = 0.002/s; (b) August 1.9 swell event, b = 0.004/s; and (c) August 13.7 swell event, b = 0.004/s. In all cases, $a_{-1}(0) = 1$, $a_1(0) = -\mathrm{i}$.

$$e^{-\Delta X/2+i\gamma|A_0|^2(1-Exp[-\Delta X])/\Delta}\left[A_0+\mu\left(a_{-1}(X)e^{-ibT}+a_1(X)e^{ibT}\right)\right] + O\left(\mu^2\right), \tag{10}$$

where $A_0 e^{-\Delta X/2+i\gamma|A_0|^2(1-Exp[-\Delta X])/\Delta}$ is an exact, Stokes-like solution of (9); the complex functions $a_{-1}(X)$ and $a_1(X)$ are the amplitudes of the minus and plus sideband perturbations with perturbation frequencies $\mp b$; and $\mu<<1$ is a small (accounting) parameter. The perturbation frequency, b, is chosen to be the one with the maximum growth rate for $\Delta = 0$. Here A_0 is a constant listed in Table 1, and the sidebands evolve with distance, X, according to

$$\begin{aligned} &i\dot{a}_1(X) - \alpha b^2 a_1 + \dot{\phi}\left[a_1 + \frac{1}{2}e^{i\phi+2iarg\{A_0\}}a^*_{-1}\right] = 0,\\ &i\dot{a}_{-1}(X) - \alpha b^2 a_{-1} + \dot{\phi}\left[a_{-1} + \frac{1}{2}e^{i\phi+2iarg\{A_0\}}a^*_{1}\right] = 0, \end{aligned} \tag{11}$$

where $\phi(X) = 2\gamma|A_0|^2\left(1-e^{-\Delta X}\right)/\Delta$; $\dot{\phi}(X) = 2\gamma|A_0|^2 e^{-\Delta X}$; $()^*$ indicates complex conjugate; and (11) results from substituting (10) into (2) and keeping only terms of $O(\mu)$.

[40] Figure 6 shows the evolution of sidebands for the three swell events of *Snodgrass et al.* [1966] discussed in section 2. The phases of the initial values of $a_{-1}(X)$ and $a_1(X)$ are chosen to give the maximum growth rate when $\Delta = 0$; the magnitudes of the initial values (of the perturbations) do not matter here, since (11) is linear. A consequence of that choice of initial phase is that $|a_{-1}(X)|$ and $|a_1(X)|$ have the same evolution. (For other choices of initial phases, the perturbation amplitudes can evolve asymmetrically, as shown by *Segur et al.* [2005].) Figure 6 shows that the presence of damping provides a bound on the growth of the perturbations. For the swell system of July 23.2, the bound is about a factor of 2.5. Thus, for this system, even though the actual decay rate of the waves is quite small (see Table 1), dissipation is likely to dominate nonlinearity in their evolution. The more appropriate measure of dissipation is its ratio to nonlinearity, δ, which for this system is 0.39 (see Table 2). For the swell system of August 1.9, the bound is much larger, about a factor of 15, and the ratio of dissipation to nonlinearity is smaller, $\delta = 0.105$. For this system, nonlinearity is likely to play an important role in evolution. Nevertheless dissipation, while not dominant, is also likely to play a role.

[41] What happens when delta is quite small, as it is for the swell systems of August 13.7 and *Collard et al.* [2009]? Figure 6c shows that for the August 13.7 swell, sideband perturbations can grow to about 60 times their original size, which is large enough for nonlinearity to dominate if the initial perturbations are not too small. (Regardless of how small delta is, one can calculate a value for the initial perturbation amplitude small enough that dissipation stops growth before nonlinearity becomes important.)

[42] For the data of *Collard et al.* [2009], the bound is larger still: (11) predicts that perturbations of wave trains like theirs grow so large that a linearized model like that in (11) is no longer relevant. Then one might suppose that the fully nonlinear model, (2), is required. But observations of large amplitude waves (with small δ) show evolution that is not governed by either (1) or (2). Instead, based on oceanographic observations of *Collard et al.* [2009], *Ardhuin et al.* [2010] concluded that swell dissipation can be nonlinear. And using laboratory data, *Segur et al.* [2005] showed that if the amplitude of either the carrier wave or the initial perturbation was large enough, the wave train exhibited a nonlinear dissipative process, *frequency downshifting*, which we discuss next.

[43] Frequency downshifting of surface water waves can occur in two different ways, which might or might not be related. The first is for wind waves. *Moskowitz* [1964], *Janssen* [2004], and others have noted that in the presence of strong enough winds, ocean waves reduce their peak frequency as they gain energy from the winds. Eventually this process stops, and the sea is called "fully developed." This process is well documented, and is not relevant for ocean swell, which propagates freely even with no wind.

[44] The second corresponds to swell, and was first documented by *Lake et al.* [1977]. They observed in laboratory experiments (with no wind) that a nearly monochromatic train of surface waves with large enough amplitudes can shift its energy to a lower frequency as it propagates. Other observations of frequency downshifting in laboratory experiments of freely propagating surface waves can be found in *Segur et al.* [2005, Figures 10–12] and *Henderson et al.* [2010, Figures 9 and 10]. Figure 4, above, shows

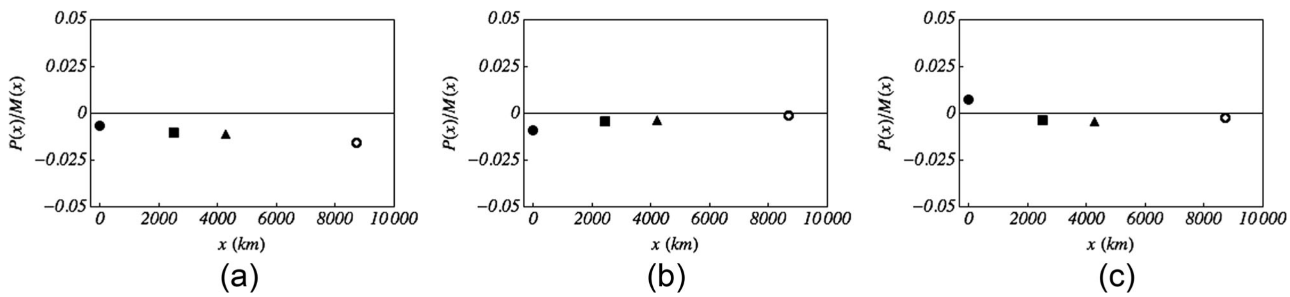

Figure 7. The ratio of momentum to energy for three swell systems of *Snodgrass et al*. [1966]. (a) July 23.2. (b) August 1.9. (c) August 13.7. The symbols are defined in Figures 3–5.

what might be the first recorded example of frequency downshifting of ocean swell.

[45] Frequency downshifting in a train of freely propagating, nearly monochromatic, dispersive waves of finite amplitude can be identified in two independent ways.

[46] 1. For a train of nearly monochromatic waves, the frequency of the carrier wave is the dominant frequency of the wave train. Downshifting occurs when the frequency of the carrier wave no longer dominates, because a lower frequency has gained more energy than that of the carrier wave. This process can be seen in Figure 4c.

[47] 2. Let $A(T,X)$ denote a solution of (9) with periodic boundary conditions (in T), and let Π denote that period. If the initial data for (9) are square-integrable, so

$$M(0) = \frac{1}{\Pi}\int_0^{\Pi} |A(T,0)|^2 dT < \infty,$$

then $A(T,X)$ has a convergent Fourier series for any $\Delta \geq 0$,

$$A(T,X) = \sum_{n=-\infty}^{\infty} a_n(X)e^{-inbT}. \quad (12)$$

Hence, a second way to define frequency downshifting is that the weighted average value of nb decreases as X increases.

[48] We now calculate this weighted average value. Two useful constants of the motion of (9) with periodic boundary conditions (in T) and $\Delta = 0$ are the wave "energy,"

$$M(X) = \frac{1}{\Pi}\int_0^{\Pi} |A(T,X)|^2 dT, \quad (13a)$$

and the "momentum"

$$P(X) = \frac{i}{\Pi}\int_0^{\Pi} [A^*\partial_T A - A\partial_T A^*]dT. \quad (13b)$$

[49] If $\Delta > 0$ in (9), then neither of these quantities is constant, but each evolves simply:

$$M(X) = M(0)e^{-\Delta X}, \quad P(X) = P(0)e^{-\Delta X}. \quad (13c, d)$$

[50] It follows that if $M(0) > 0$, then

$$\frac{P(X)}{M(X)} = \frac{P(0)}{M(0)} \quad (13e)$$

is a constant of the motion in (9), for any $\Delta \geq 0$. Making use of (12) and Parseval's relation [e.g., *Guenther and Lee*, 1988], we may write

$$M(X) = \sum_{n=-\infty}^{\infty} |a_n(X)|^2, \quad P(X) = 2\sum_{n=-\infty}^{\infty} nb|a_n(X)|^2. \quad (14)$$

[51] If one interprets $|a_n(X)|^2$ as a non-normalized probability density, then it follows from (14) that $P(X)/M(X)$ is twice the average frequency of any solution of (9) with periodic boundary conditions. And it follows from (13e) that this average frequency is a constant of the motion of (9), for any $\Delta \geq 0$. Thus, according to the second definition of frequency downshifting, above, *no bounded solution of (9) with periodic boundary conditions can exhibit downshifting, for any* $\Delta \geq 0$.

[52] A similar argument applies to solutions of (1) or (2) with periodic boundary conditions in (ξ, η). In that case, $P(\tau)$ becomes a two-component vector, corresponding to the two directions (ξ, η). For one of these two components, $P(\tau)/M(\tau)$ represents twice the average frequency of the solution of (1) or (2), and it is a constant of the motion. Therefore, according to the second definition of frequency downshifting (above), *downshifting lies outside of the range of validity of either (1) or (2) as approximate models of the evolution of ocean swell*.

[53] One can show by a similar argument that downshifting also lies outside the range of validity of a higher-order NLS-type model due to *Dysthe* [1979]. Note that all of these results depend on using the second definition of downshifting, not the first. For the laboratory experiments of *Segur et al*. [2005] or *Henderson et al*. [2006, 2010], it was not necessary to distinguish between these two definitions of downshifting, because we saw no experiments in which one of these occurred while the other did not. Fewer data are available for ocean swell, so we cannot guarantee that the two definitions always agree.

[54] Figure 7 shows the measured evolution of $P(X)/M(X)$ for the three sets of swell from *Snodgrass et al*. [1966], discussed in section 2. Note that for the August 13.7 swell system, $P(X)/M(X)$ decreases and changes sign between Tutuila (at $X = 0$) and Palmyra (at $X = 2400$ km). The decrease of $P(X)/M(X)$ shows that (13e) was not satisfied during this interval, but $P(X)$ and $M(X)$ are both obtained from field data, so perhaps this decrease is due only to scatter in those data. The change of sign of $P(X)/M(X)$ is more serious. According to (13a), $M(X)$ must remain non-negative, and the data in Figure 4 show that

$M(X)$ decreased as X increased. So if $P(X)/M(X)$ changed sign, then $P(X)$ changed sign, and the evolution of $P(X)$ is badly predicted by (13d). We conclude that the August 13.7 swell system underwent frequency downshifting, according to the second definition above. In fact, the August 13.7 swell system also downshifted according to the first definition above—the data in Figure 4c show that the spectral peak of this swell system downshifted between Tutuila and Palmyra.

[55] For the swell systems observed by *Collard et al*. [2009], the measure of nonlinearity, ε, was almost three times that for the August 13.7 event. Hence, we would expect the ratio $P(X)/M(X)$ decrease for these waves as well, but with no measurements of $P(X)$ or $M(X)$ for the swell of *Collard et al*. [2009], we cannot test the hypothesis. Nevertheless the conclusion of *Ardhuin et al*. [2009, 2010], that swell dissipation is amplitude dependent, is consistent with the occurrence of frequency downshifting in their data, because *Islas and Schober* [2011] found that adding nonlinear damping to an NLS-type numerical code leads to what they call "irreversible downshifting."

[56] Possible explanations for downshifting of freely propagating surface waves are discussed by *Dias and Kharif* [1999], based primarily on numerical computations. To our knowledge, these results have not yet been verified experimentally. The cause of downshifting is less clear for ocean swell than it is for waves in the laboratory, because ocean swell can gain or lose energy through interactions with local seas, winds and currents, whereas these other possibilities can be excluded from laboratory experiments.

[57] The results of sections 2 and 3 show that dissipation can play a significant role in the evolution of ocean swell. Dimensional decay rates of swell are much smaller than those in laboratory experiments, but nonlinearity can also be much smaller in swell than in a laboratory. The ratio of dissipative to nonlinear effects, δ (see Table 2), provides a measure of the relative importance of these competing effects. The values of δ obtained from observations of ocean swell are large enough to indicate that dissipation is not negligible for evolution. Indeed, dissipation can inhibit the growth of perturbations of swell, and even stop their growth in some cases. In section 4, we consider sources and models for dissipation.

[58] Another stabilizing mechanism, first studied by *Alber* [1978], is randomness in the wave field, which might have played a role in stabilizing the swell systems discussed here. Alber's work showed that the relative strength of nonlinearity versus spectral bandwidth, measured by the Benjamin-Fier Index (BFI), determines whether randomness in the surrounding wave field can lead to instability of a uniform wave train: as the nonlinearity increases or the spectral bandwidth decreases, the likelihood of an instability increases.

[59] In Alber's work, the BFI is constant over the wave field, but a swell wave train undergoes dispersive spreading as the waves propagate, so the spectral bandwidth in the direction of propagation of the wave train necessarily decreases over time. Mathematically, one can show that this bandwidth should decrease like *1/D*, where D is the distance the wave train has propagated from its source. Practically, this decreasing bandwidth played such an important role in the analysis of swell by *Snodgrass et al*. [1966] that they mention it in the abstract of their paper. A consequence is that the BFI almost certainly increases as the wave train propagates, making it less and less likely that randomness could stabilize a propagating train of swell.

[60] A second problem with applying Alber's work to a dispersing swell wave train is that the theory requires that the wave field be spatially homogeneous. But a swell wave train is certainly not spatially homogeneous: longer waves travel faster than shorter waves, so a snaphot of the wave field at any fixed time (after the waves have propagated away from the source) shows clearly the direction in which the wavefield is propagating. With more work, one can estimate from this same snapshot the size of D—the distance back to the source of the wavefield.

[61] Thus, Alber's work does not apply to swell such as that analyzed by *Snodgrass et al*. [1966] or *Collard et al*. [2009]. Indeed, to obtain a spatially homogeneous wave state, *Komen et al*. [1984] "... ensured that no swell was present ... ." Nevertheless, we cannot rule out the possibility that both randomness and dissipation played a role in stabilization of the observed swell.

4. Approximate Models of Ocean Swell in the Presence of Dissipation

[62] Comparisons in section 2 of data from ocean swell and from laboratory experiments show that measured dissipation rates in the open ocean are vastly smaller than those in a laboratory wave tank. Even so, the comparisons in sections 2 and 3 show that the role of dissipation in the evolution of ocean swell can be comparable to its role in the evolution of surface water waves in a laboratory wave tank. The objective of this section is to examine possible theoretical models of dissipation for small-amplitude waves.

[63] Waves in a laboratory wave tank experience dissipation in the boundary layers on the sidewalls and bottom of the tank, but the observed decay rates of gravity-driven surface waves are often larger than what can be attributed to these boundary layers. No such boundary layers affect ocean swell on deep water, but ocean swell clearly loses energy as it propagates, as shown in section 2.

[64] At this time, we do not know what mechanism generates the "extra" dissipation in laboratory wave trains, nor the mechanism that generates dissipation of ocean swell on deep water, nor whether the same mechanism is at work in both situations. For surface water waves, maximum velocities occur on the free surface, and so do maximum velocity gradients (away from rigid boundaries) so there is reason to expect the "extra" dissipation to occur near the free surface. In this section, we consider four boundary conditions, each of which has been proposed to allow for viscous dissipation at or near the free surface, and we give the dissipation rate predicted by that model for infinitesimal waves. By comparing the dissipation rates predicted by each of these mathematical models with the observed dissipation rates of laboratory-generated waves and of ocean swell, we hope to narrow the range of plausible mechanisms that create the observed dissipation, in wave tanks and in the open ocean.

4.1. Boundary Layers on the Sidewalls and Bottom of a Wave Tank

[65] We begin with a known source of dissipation, along the sidewalls and bottom of a wave tank. The dissipation from these boundary layers is well understood and does not affect ocean waves on deep water. Consider a long wave tank with a rectangular cross section of width W, filled to a depth h with still water. A wave maker, which spans the width at one end of the tank, creates a train of periodic, plane waves of small amplitude a, which then propagate to the other end of the tank. Either the waves are absorbed at the other end, or else the experiment ends when the wave train first reaches the far end of the tank; either way, we assume that all of the waves propagate in one direction, with no reflected waves. We also assume that the fluid motion is nearly irrotational, and that the wavelength of these waves is long enough that surface tension can be ignored. Then the frequency ω and the wave number k of the waves are related by the usual dispersion relation for gravity-driven surface waves with small amplitudes,

$$\omega^2 = gk \tanh(kh). \tag{15}$$

[66] The energy of a packet of these waves travels with the group velocity,

$$C_g = \frac{g[2kh + \sinh(2kh)]}{4\omega\cosh^2(kh)}. \tag{16}$$

[67] As the waves propagate, they create oscillatory boundary layers on the sidewalls and bottom of the tank. The rotational motion inside these boundary layers dissipates energy. The spatial decay rate of the amplitude of this uniform wave train, due to these boundary layers, is well established [*Van Dorn*, 1966]:

$$\frac{\Delta_{Wh}}{2} = \left(\frac{\nu}{2\omega}\right)^{1/2}\left(\frac{2k}{W}\right)\left(\frac{kW + \sinh(2kh)}{2kh + \sinh(2kh)}\right), \tag{17}$$

where ν is the kinematic viscosity of water. If the boundary layers on the sidewalls and bottom of the tank were the only sources of dissipation, then the elevation of the free surface above its quiescent level for a small-amplitude wave train would be

$$\eta(x,t) = a\,\exp\left\{-\frac{\Delta_{Wh}}{2}x\right\}\sin\{kx - \omega t + \theta_0\} + O\left(a^2\right). \tag{18}$$

[68] As a concrete example, consider the experiment of *Segur et al*. [2005], cited in Table 2: tank width, $W = 0.254$ m; water depth, $h = 0.20$ m; wave frequency, $\omega/2\pi = 3.33$ Hz; wave number, $k = 44.1$ m^{-1}; kinematic viscosity of water at 20°C, $\nu = 1.00 \times 10^{-6}$ m^2/s. Then (17) gives a spatial decay rate for wave amplitudes due to boundary layers at the sidewalls and bottom of the tank:

$$\Delta_{Wh}/2 = 0.054\,\mathrm{m}^{-1}. \tag{19}$$

[69] This is approximately half of $\Delta/2 = 0.11$ m^{-1}, the amplitude-decay rate measured by *Segur et al*. [2005]. Thus, the dissipation from wall boundary layers is important in laboratory experiments, but they might not be the only source of dissipation. For ocean swell propagating on deep water, there are no sidewalls and the bottom boundary layer is insignificant, so none of the dissipation predicted by (17) occurs.

[70] Each of the four models discussed below provides a prediction of dissipation due to viscous effects at or near the free surface. For laboratory experiments, this decay rate should be added to that from (17).

4.2. The Clean-Surface Model

[71] This model, consisting of a viscous fluid beneath a free surface, with a vacuum above the surface, was explored in detail in *Lamb* [1932, section 349] and has been popular. *Dias et al*. [2008] used it to derive (2) from the Navier-Stokes equations, with an explicit formula for the decay rate, given below in (21b). *Lo and Mei* [1985] assert that this model provides the viscous-damping factor "in the open ocean or a very wide tank."

[72] The model consists of the Navier-Stokes equations for an incompressible, viscous fluid of infinite depth, bounded above by a free surface, with a vacuum above that surface. A constant gravitational force acts downward; one can also include surface tension, but we neglect it here. One can obtain a dissipation rate by linearizing the equations, which simplifies the problem. For a two-dimensional fluid flow, one uses a Helmholtz decomposition to write the velocity field with an irrotational part and a rotational part. Thus, for a wave motion with (real-valued) spatial wave number k, the two components of velocity are

$$\begin{aligned} u(x,z,t) &= ik\left[Ae^{ikx+\sigma t} - A^*e^{-ikx+\sigma^* t}\right]e^{-|k|z} \\ &\quad -\left[mCe^{ikx+\sigma t+mz} + m^*C^*e^{-ikx+\sigma^* t+m^* z}\right], \\ w(x,z,t) &= |k|\left[Ae^{ikx+\sigma t} + A^*e^{-ikx+\sigma^* t}\right]e^{|k|z} \\ &\quad +ik\left[Ce^{ikx+\sigma t+mz} - C^*e^{-ikx+\sigma^* t+m^* z}\right], \end{aligned} \tag{20a, b}$$

where we require

$$Re(m) > 0 \tag{20c}$$

so that the motion vanishes as $z \to -\infty$. The first terms in each line of (20a, 20b) satisfy the Laplace equation, and the second terms in each line satisfy the linear diffusion equation, so

$$\sigma = \nu\left(m^2 - k^2\right), \tag{20d}$$

where ν is the kinematic viscosity of the fluid. One also needs to represent the pressure in the liquid, and the (moving) location of the free surface ($z = \eta(x,t)$). Then on the free surface, one must satisfy a kinematic condition ($\partial_t\eta = w|_{z=\eta}$) and two dynamic conditions (that the normal and tangential components of stress both vanish on $z = \eta$). After some algebra, one obtains a quartic equation for $\{m/|k|\}$. This equation has two roots with $Re(m) > 0$. For $g = 9.81$ m/s^2, $\nu = 1.00 \times 10^{-6}$ m^2/s, and waves long enough that one can ignore surface tension, these two roots correspond to waves traveling to the left and to the right.

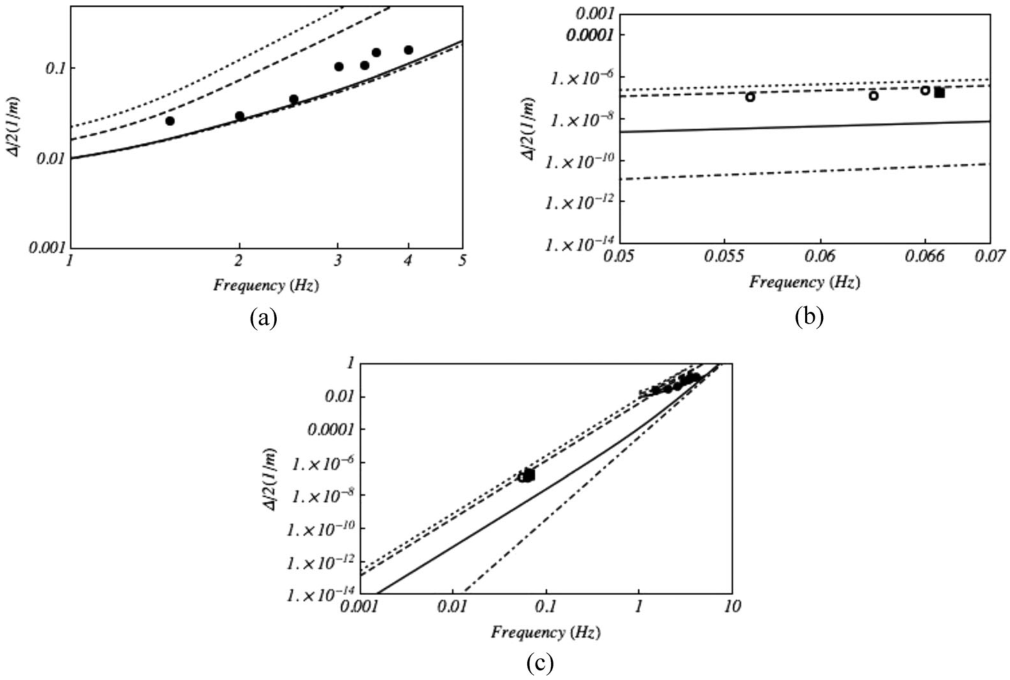

Figure 8. Spatial decay rates of wave amplitude for freely propagating surface water waves, in laboratory experiments (in Figures 8a and 8c) and for ocean swell (Figures 8b and 8c). In all graphs, the symbols represent observed decay rates, either in our lab (for Figure 8a) or in the ocean (for Figure 8b). In Figure 8b, hollow circles represent data from *Snodgrass et al*. [1966], while the solid square represents the result from *Collard et al*. [2009]. In all graphs, the dashed-dotted curve shows predictions of the clean-surface model, the solid curve shows predictions of the two-fluid model, the dashed curve shows predictions of the inextensible surface model, and the dotted curve shows predictions of maximum decay rate from the surfactant model. The curves in Figure 8a include the contributions of boundary layers on the walls and bottom of a tank, while the curves in Figure 8b exclude those contributions. Figure 8c combines the two graphs into a single figure.

Substituting either of these roots into (20d) yields a bound on the temporal dissipation rate:

$$\mathrm{Re}(\sigma) \leq 2\nu k^2. \tag{21a}$$

With an error of less than 1% for any surface water wave with frequency less that 3 Hz,

$$\mathrm{Re}(\sigma) \approx 2\nu k^2. \tag{21b}$$

The spatial decay rate is obtained by dividing (21b) by C_g so that we may approximate

$$\frac{\Delta_{cs}}{2} \approx 4\frac{\nu k^3}{\omega} = 4\frac{\nu}{\sqrt{g}}|k|^{5/2}. \tag{22}$$

[73] We note that this model does not impose a boundary layer structure on the problem—the only approximation is to linearize the Navier-Stokes equations. For small Δ_{cs}, *Re* $(m/|k|)$ is small, so the rotational motion is usually confined to a thin layer near the free surface. But this is a consequence of the dynamics, not because it is imposed on the problem.

[74] Again, we use the parameters of the laboratory experiment cited in Table 2 as an example, to obtain a predicted amplitude-decay rate due to dissipation at the free surface of $\Delta_{cs}/2 = 0.016\ \mathrm{m}^{-1}$. Add this to the decay-rate from sidewall and bottom boundary layers (in (19)) to obtain the amplitude-decay rate predicted by the clean-surface model:

$$\Delta/2 = 0.070\,\mathrm{m}^{-1}. \tag{23}$$

[75] The dashed-dotted line in Figure 8a shows the prediction of (17) plus (22), while (22) by itself gives the dotted line in Figure 8b. (For the experiments in Figure 8a, $h = 0.20$ m and $W = 0.254$ m. The surface was cleaned by blowing a wind that pushed the surface film to one end of the tank where it was vacuumed away. The wave maker is described in *Segur et al*. [2005].)

4.3. The Two-Fluid Model

[76] *Dore* [1978] noted that for waves at the air-water interface, the decay rate predicted by the clean-surface model "is a good approximation only for waves whose period is a small fraction of a second," but it is very often used for waves of much longer periods, with poor results. Dore addressed this deficiency by accounting for viscous dissipation both in the water below the air-water interface and in the air above it. Somewhat surprisingly, he found that for ocean swell, most of the dissipation occurs not in the water but in the air! At atmospheric pressure and 20°C,

the density of water is about 800 times heavier than that of air, but the kinematic viscosity of air is about 15 times larger than that of water. As a result, the dissipation rate predicted by this model can be significantly different from that of the clean-surface model, which is a limiting case of *Dore*'s [1978] model.

[77] Logically, the two-fluid model is a direct generalization of the clean-surface model. One considers two immiscible, incompressible, viscous fluids, with the lighter one resting above the heavier one, and a movable interface between them. Both are influenced by a constant gravitational field. In the simplest situation, each fluid fills a semi-infinite region, but there are nearly twice as many variables as in the clean-surface model, and the problem is not very simple, even after linearizing the equations and restricting to two-dimensional motion. Each fluid has a velocity field with a rotational and irrotational part, like that in (20); there are two kinematic boundary conditions at the interface, relating the motion of the interface to the normal velocity in each fluid at the interface; the dynamic boundary conditions at the interface are that both the normal and tangential components of stress must be continuous across the interface. This model reduces to the clean-surface model if one sets the density and dynamic viscosity of the upper fluid to zero.

[78] *Dore* [1978] does not actually solve this linearized problem. Instead he works out what he calls "an excellent numerical approximation" for the spatial decay rate of wave amplitudes, according to this model:

$$\frac{\Delta_{2f}}{2}=\left[\sqrt{2}\frac{\rho_a}{\rho_w}\left(\nu_a k^2\right)^{1/2}(g|k|)^{1/4}+2\nu_w k^2\right]\left(2\sqrt{\frac{|k|}{g}}\right), \tag{24}$$

where $\{\rho_{\mathrm{a}}, \nu_{\mathrm{a}}; \rho_{\mathrm{w}}, \nu_{\mathrm{w}}\}$ refer to the density and kinematic viscosity of air and water, respectively. In (24), the first term in the square brackets represents dissipation in the air, while the second term reproduces (21b) and represents dissipation in the water. For the experiment cited in Table 2, with $\rho_{\mathrm{a}}/\rho_{\mathrm{w}}=0.0012$, $\nu_{\mathrm{a}}=15.3\ \mathrm{m}^2/\mathrm{s}$, (24) gives $\Delta_{2f}/2=0.022\ \mathrm{m}^{-1}$. When added to (19), this gives the amplitude-decay rate predicted by the two-fluid model for this particular experiment:

$$\Delta/2=0.076\,\mathrm{m}^{-1}. \tag{25}$$

[79] For this experiment, most of the dissipation occurred on the sidewalls and bottom of the tank, given by (20); at the free surface, there was more dissipation in the water (the second term in (24)) than in the air (the first term in (24)). But for the long wavelengths seen in ocean swell, this ordering is reversed—there are no sidewalls, and almost all of the dissipation occurs in the air. The solid curves in Figure 8 show the predictions of the two-fluid model, added to (17) for Figure 8a, and by itself in Figure 8b.

4.4. An Inextensible-Film Model

[80] In this model a viscous, incompressible fluid lies beneath a free surface (at $z=\eta(x,t)$) under the force of (constant) gravity. The velocity field of the fluid has a rotational part and an irrotational part, given by (20a) and (20b) in the linearized problem. One imposes the usual (linearized) kinematic condition at the free surface ($\partial_t\eta = w|_{z=\eta}$). The normal stress at the free surface is required to vanish, as in the clean-surface model. The essential feature of this model is that a thin, massless film, lying on the free surface, cannot stretch tangentially, and a no-slip condition on that surface forces the tangential velocity of the fluid to vanish there. The tangential stress at the free surface is not constrained, and it is usually not zero.

[81] *Lamb* [1932, section 351] analyzes this model for an infinitely deep fluid and derives a decay rate for this linearized problem. His result leads to the following spatial decay-rate for wave amplitudes:

$$\frac{\Delta_{\mathrm{film},\infty}}{2}=k^2\sqrt{\frac{\nu}{2\omega}}=\sqrt{\frac{\nu}{2}}\frac{k^2}{(g|k|)^{1/4}}. \tag{26a}$$

(Lamb's analysis in section 351 is similar to that of the clean-surface model in section 349. His work requires some decoding, because he uses a parameter α without defining it: α in section 351 is the complex frequency, denoted by n in page 349.)

[82] The generalization of (26a) for a fluid of finite depth h is

$$\frac{\Delta_{\mathrm{film},h}}{2}=\sqrt{\frac{\nu}{2\omega}}\left[\frac{2k^2\cosh^2(kh)}{2|k|h+\sinh(2|k|h)}\right], \tag{26b}$$

where ω is given by (15). *Miles* [1967] gives results consistent with this, but does not give (26b) explicitly. Equation (4) of *Van Dorn* [1966] is similar to (26b), but it contains misprints. See the Appendix for a derivation of (26b).

[83] To use this model to predict an amplitude-decay rate in a wave tank, one should add the results from either (26a) or (26b) to that from (17). As an example, $kh=8.82$ for the lab experiment cited in Table 2, and (26a and 26b) both predict a decay-rate due to dissipation near the free surface of $\Delta_{\mathrm{film}}/2=0.30\ \mathrm{m}^{-1}$. Adding this to (17) gives the amplitude-decay rate predicted by the inextensible-film model for this experiment:

$$\Delta/2=0.35\,\mathrm{m}^{-1}. \tag{27}$$

[84] Thus, while the clean-surface model (in (22)) and the two-fluid model (in (24)) both predict amplitude-decay rates less than the measured value ($\Delta/2=0.11\ \mathrm{m}^{-1}$), the inextensible-film model predicts a decay rate larger than the measured value.

[85] This pattern persists for all of the data available to us. Figure 8a shows amplitude-decay rates measured in our wave channel for wave trains with frequencies between 1.5 and 4 Hz. The dashed curve represents the inextensible-film model, with results from either of (24a and 24b) added to the prediction of (17). It consistently predicts values higher than either the two-fluid model (represented by the solid curve) or the clean-surface model (the dashed-dotted curve), and also higher than the measured values. Figure 8b shows measured amplitude-decay rates for ocean swell, based on observational data from *Snodgrass et al.* [1966] and *Collard et al.* [2009]. The dashed curve, representing

the inextensible-film model, predicts values higher than those observed, while the two-fluid model (solid curve) and the clean-surface model (dashed-dotted curve) both predict values less that those observed. The inextensible film model is less accurate than either the clean-surface model or the two-fluid model in predicting the laboratory data, but it is the most accurate predictor of the ocean data. The clean-surface model has been used more than the other two models considered herein, but it predicts the decay of ocean swell poorly.

[86] Figure 8 makes the inextensible-film model attractive, so it might be worthwhile to point out a limitation of that model. Both the clean-surface model and the two-fluid model are posed as nonlinear models; we linearize them to find their (linearized) dissipation rates, quoted above, but there is no conceptual problem in going beyond linearized models to find approximate nonlinear models for surface waves on a viscous fluid.

[87] In contrast, the inextensible surface model is intrinsically linear—the condition that the tangential velocity should vanish on the interface can hold *only* in a linearized model. To see this, note that for a free surface given by ($z = \eta(x,t)$), the unit normal vector is

$$\hat{n} = \frac{(-\partial_x \eta, 1)}{\sqrt{1 + (\partial_x \eta)^2}}.$$

[88] So the kinematic boundary condition on the free surface,

$$\partial_t \eta + u \partial_x \eta = w,$$

[89] can also be written in a form due to *Zakharov* [1968],

$$\partial_t \eta = v_n \sqrt{1 + (\partial_x \eta)^2}, \tag{28}$$

where $v_n = (u, w) \cdot \hat{n}$ is the normal component of fluid velocity on the surface. It follows from (28) that the vertical motion of the free surface ($\partial_t \eta$) is usually greater than the normal component of fluid velocity, so the extra velocity must come from the tangential velocity, which therefore cannot be zero. This argument holds everywhere on the free surface, except where $\partial_x \eta = 0$ or $v_n = 0$.

[90] Thus, the limitation of the inextensible-film model is that it is incomplete—it does not uniquely identify its nonlinear generalizations. It is likely that many nonlinear models reduce to the inextensible-film model when linearized.

4.5. A Visco-Elastic Film Model

[91] In this model, a visco-elastic film at the surface has its own constitutive law and dynamics. The stress in the film must balance the stress in the fluid at the interface. *Miles* [1967] gives a review of the derivation and shows that the inextensible-film model discussed in section 4.3 is the limit of infinite elasticity for an insoluble film. Thus, predictions from the visco-elastic film model agree with measurements of linear decay in the appropriate limits (of infinite elasticity and infinitesimal amplitude). But the visco-elastic film model does not share the inextensible-film model's inherent problem of intrinsic linearity. So the former is a candidate for a model that agrees with measurements at linear order and can be used to study dynamics occurring at higher order.

[92] However, finite elasticity admits longitudinal waves in the film, which can resonate with the water wave, causing dissipation that is larger than the inextensible film limit. Miles found the maximum damping rate due to this resonance to be twice that of the inextensible-film model. *Huhnerfuss et al*. [1985] also discuss the visco-elastic model. In their notation, the limiting value of dissipation for gravity waves is

$$\frac{\Delta_{ve,max}}{2} = \sqrt{2}\left[\frac{\nu^2 k^7}{g}\right]^{1/4}, \tag{29}$$

which is twice that of the inextensible-film model (26a). Figure 8 also includes this prediction with the dotted curve. It does not appear to be relevant for the laboratory case where we clean the surface, however, it provides an upper bound on the dissipation rate for ocean swell.

[93] Finally, we note that no model for linear decay rates will explain amplitude-dependent dissipative effects such as those observed by *Ardhuin et al*. [2010]. Can linear decay rates account for frequency downshifting? All of the predictions of decay rate discussed in this section depend on the wave frequency. In derivations of dissipative nonlinear Schrödinger-type equations like (2) for deepwater wave evolution, the decay rate that appears [e.g., *Dias et al*., 2008] will depend only on the frequency of the carrier wave. Nevertheless, one wonders: if the sidebands were free waves and were allowed to decay at their own rates, would the most unstable minus and plus sidebands have significantly different amplitudes at say, half the propagation distance? For the laboratory, both the Dore model and the clean-surface model, plus the contributions from the sidewall and bottom boundary layers, predict measurements reasonably well. Using these models to examine frequency dependence, we find that the ratio of the amplitude of the minus sideband to the amplitude of the plus sideband, if initially equal, stays equal (to within four decimal places) for the length of the wave tank. (This result is unchanged using the inextensible-film model.) Indeed, the data show for moderate amplitude waves, the minus secondary and tertiary sidebands may grow at a *slower rate* than the plus secondary and tertiary sidebands, depending on initial phases [see *Segur et al*., 2005, Figure 6]. This asymmetric growth is well predicted by (2). *So, linear dissipation alone cannot account for frequency downshifting in the laboratory experiments*. For ocean swell, the inextensible-film model best predicts measurements. Using that model with the carrier and most unstable sideband frequencies corresponding to the August 13.7 swell, the ratio of minus to plus sideband amplitudes at 5000 km (about half the propagation distance) is 1.12, so there is a measurable difference in the amount that the two sidebands decay. This effect provides another cause of frequency downshifting for ocean swell that is not present for laboratory waves. It will not be present in models that assume a single, representative decay rate for the entire spectrum, indicating a potential limitation of such models.

5. Summary

[94] In this paper, we considered the effects of dissipation on the evolution of ocean swell. Decay rates obtained from observations of ocean swell are orders of magnitude smaller than decay rates of necessarily higher frequency waves in a laboratory. However, the swell is also typically much less nonlinear than the laboratory waves. So, the relative strength of dissipation versus nonlinearity for the laboratory and the ocean are not so disparate. Therefore, information gained from laboratory experiments may have some relevance to ocean swell. We further examined this idea by considering the dissipative growth of small perturbations for ocean swell and found that for swell with small enough nonlinearity, dissipation impedes and can stop this modulational instability before sidebands grow appreciably.

[95] As shown in Figure 4, for one observed swell system with larger nonlinearity, frequency downshifting occurred. Downshifting is not predicted by models of narrow-banded, freely propagating deep water waves derived from Euler's equations such as nonlinear Schrödinger-type models (including higher order in bandwidth models) even if linear dissipation is included.

[96] The type of dissipation we examined here, with exponential decay, agrees well with observations in the laboratory and in the ocean. Predicting the actual measured decay rate is more difficult. We examined predictions from four models, which use (i) a stress-free surface above a viscous fluid, (ii) a continuous-stress interface between two viscous fluids (air and water), (iii) no constraint on tangential stress, but zero tangential velocity at the surface, and (iv) continuity between stress in the water and stress in a visco-elastic film on the interface. We compared predictions from these models with observations and found that (iii) agrees well with measurements of decay rates of ocean swell. Its constraint of no tangential flow at the surface is incorrect for nonlinear waves and, therefore, cannot be used to derive a model with nonlinear dissipation. However, it is a limit of the model (iv), which does not have that constraint.

[97] The main conclusion of this paper is that viscous dissipation, which usually has only a weak effect on the propagation of surface water waves forced by gravity, can affect the stability of those waves. It does so for ocean swell because dissipation and nonlinear interactions occur on the same time scale. This overlapping of time scales is inherent in equation (2).

Appendix A: Derivation of (26b)

[98] Consider a viscous, incompressible fluid, subject to a constant gravitational force, g, which acts vertically downward. The fluid rests on a flat, horizontal bed at $z=-h$, and is bounded above by a free surface at $z=\eta(x,t)$. We restrict our attention to two-dimensional motion, and linearize the equations of motion. Then a sinusoidal wave of amplitude $2|N|$ and wave number k appears on the free surface as

$$\eta(x,t) = N\ e^{ikx+\sigma t} + N^* e^{-ikx+\sigma^* t}, \tag{A1}$$

where $\sigma(k)$ is a complex-valued frequency to be determined, and $(\ )^*$ denotes complex conjugate. The two-dimensional velocity field has a Helmholtz decomposition:

$$u = \partial_x\phi - \partial_z\psi, \quad w = \partial_z\phi + \partial_x\psi, \tag{A2a, b}$$

in which the velocity potential, $\phi(x,z,t)$, and the stream function, $\psi(x,z,t)$, satisfy, respectively,

$$\partial_x^2\phi + \partial_y^2\phi = 0, \quad \partial_t\psi = \nu\left[\partial_x^2\psi + \partial_y^2\psi\right], \tag{A2c, d}$$

and $\nu > 0$ is the kinematic viscosity of the fluid. For a traveling wave, the velocity potential and the stream function must be of the form:

$$\begin{aligned}\phi(x,z,t) &= Ae^{ikx+\sigma t}\frac{\cosh\{k(z+h)\}}{\cosh\{kh\}}\\ &+A^* e^{-ikx+\sigma^* t}\frac{\cosh\{k(z+h)\}}{\cosh\{kh\}},\\ \psi(x,z,t) &= Be^{ikx+\sigma t}\sinh\{m(z+h)\}\\ &+B^* e^{-ikx+\sigma^* t}\sinh\{m^*(z+h)\}.\end{aligned} \tag{A2e, f}$$

[99] As in section 4, we require that $Re\ (m(k)) > 0$, so that the maximum velocity occurs at the free surface, and that $\{\sigma,m,k\}$ are related by (20d).

[100] The linearized momentum equations imply that the pressure in the fluid satisfies

$$\frac{p(x,z,t)}{\rho} + gz + \partial_t\phi = \text{constant},$$

and we may set the constant to zero without loss of generality.

[101] Three boundary conditions must be satisfied at the free surface.

[102] 1. The kinematic condition, that $\partial_t\eta = w|_{z=0}$, yields

$$-i\sigma N = k\tanh(kh)A + ik\sinh(mh)B. \tag{A3a}$$

[103] 2. The condition of no tangential motion along the free surface defines this model:

$$ikA - m\cosh(mh)B = 0. \tag{A3b}$$

[104] 3. The balance of normal stress at the free surface:

$$\begin{aligned}&\frac{p}{\rho} = -g\eta - \partial_t\phi|_{z=0} = 2\nu\partial_z w|_{z=0}\\ &=> -gN + i\sigma A = 2\nu k^2 A + 2i\nu km\cosh(mh)B.\end{aligned} \tag{A3c}$$

[105] Equations (A3a,b,c) have nonzero solutions only if

$$m\left[\sigma^2 + gk\tanh(kh)\right] - gk^2\tanh(mh) = 0. \tag{A4}$$

[106] Equations (A4), (15c), and (15d) determine both $m(k)$ and $\sigma(k)$. Use (20d) to eliminate σ^2 from (A4). After some rearrangement, the result can be written as

$$(m-|k|)\left[\nu^2 m(m-|k|)(m+|k|)^2 + g|k|\left\{\frac{m\tanh(|k|h)-|k|\tanh(mh)}{m-|k|}\right\}\right]=0. \tag{A5}$$

[107] One solution of (A5) is $\{m=|k|\}$, so $\sigma=0$ from (20d). This solution describes a static solution of the Laplace equation, with no motion. For $m\neq|k|$, define

$$z=\frac{m}{|k|},\ \lambda^4=\frac{g|k|}{(\nu k^2)^2},\ \Lambda^4=\frac{g|k|\tanh(|k|h)}{(\nu k^2)^2}. \tag{A6}$$

Then the second factor in (A5) yields

$$z(z-1)(z+1)^2+\lambda^4\left\{\frac{z\tanh(|k|h)-\tanh(z|k|h)}{z-1}\right\}=0, \tag{A7}$$

while (20c) implies $Re(z)>0$.

[108] For $\nu=10^{-6}$ m^2/s (for water), $g=9.81$ m/s^2, and wavelengths longer than 5 cm, $\lambda^4>10^{18}$. For $\lambda^4>>1$ and $\lambda|k|h>>1$, $z=$O(λ), so

$$\left\{\frac{z\tanh(|k|h)-\tanh(z|k|h)}{z-1}\right\}\sim\frac{z\tanh(|k|h)-1}{z-1} = \tanh(|k|h)-\frac{1-\tanh(|k|h)}{z-1}.$$

In this range, (A7) has two solutions consistent with (20c), given approximately by

$$z_\pm=\left(\Lambda e^{\pm i\pi/4}\right)-\frac{\coth(|k|h)}{4}+O\left(\Lambda^{-1}\right). \tag{A8}$$

Substituting (A8) into (20d) after using (A6) determines $\sigma(k)$:

$$\sigma_\pm=\pm i\sqrt{gk\tanh(kh)}-\frac{1\pm i}{2\sqrt{2}}\sqrt{\nu k^2}(gk\tanh(kh))^{1/4}\coth(|k|h) + O(1),$$

corresponding to waves that propagate to the left or right, and that decay in time. At leading order, the temporal frequency of oscillation is given by (15), and the temporal decay rate is

$$-\frac{\coth(|k|h)}{2\sqrt{2}}\sqrt{\nu k^2}(gk\tanh(kh))^{1/4}.$$

The spatial decay rate at leading order is obtained by dividing this by the group velocity, given in (16). The result is given in (26b).

[109] **Acknowledgments.** This work was supported in part by the National Science Foundation, DMS-1107379 and DMS-1107354. We are grateful for helpful discussions with John Miles, Ken Melville, C. C. Mei, Chris Garrett, and Walter Munk.

References

Ablowitz, M. J., and H. Segur (1979), *Solitons and the Inverse Scattering Transform*, 391 pp., Soc. for Ind. and Appl. Math., Philadelphia, Pa.

Alber, I. E. (1978), The effects of randomness on the stability of two-dimensional surface wavetrains, *Proc. R. Soc. London*, Ser. A, *363*, 525–546.

Ardhuin, F., C. Bertrand, and F. Collard (2009), Observation of swell dissipation across oceans, *Geophys. Res. Lett.*, *36*, L06607, doi:10.1029/2008GL037030.

Ardhuin, F., et al. (2010), Semiempirical dissipation source functions for ocean waves. Part I: Definitions, calibration and validation, *J. Phys. Oceanogr.*, *48*, 1917–1941, doi:10.1175/2010JPO4324.1.

Benjamin, T. B., and J. Feir (1967), The disintegration of wave trains on deep water, *J. Fluid Mech.*, *27*, 417–430.

Benney, D. J., and A. C., Newell (1967), The propagation of nonlinear wave envelopes, *J. Math. Phys. (Stud. Appl. Math.) 46*, 133–139.

Calini, A., and C. M. Schober (2002), Homoclinic chaos increases the likelihood of rogue waves, *Phys. Lett. A*, *298*, 335–349.

Collard, F., F. Ardhuin, and B. Chapron (2009), Monitoring and analysis of ocean swell fields from space: New methods for routine observations, *J. Geophys. Res.*, *114*, C07023, doi:10.1029/2008JC005215.

Dean, R. G., and R. A. Dalrymple (1991), *Water Wave Mechanics for Engineers and Scientists*, 344 pp., World Sci., Singapore.

Dias, F., and C. Kharif (1999), Nonlinear gravity and capillary-gravity waves, *Ann. Rev. Fluid Mech.*, *31*, 301–346.

Dias, F., A. I. Dyachenko, and V. E. Zakharov (2008), Theory of weakly damped free surface flows: A new formulation based on potential flow solutions, *Phys. Lett. A*, *372*, 1297–1302.

Dore, B. D. (1978), Some effects of the air-water interface on gravity waves, *Geophys. Astrophys. Fluid Dyn.*, *10*, 213–230.

Dyachenko, A. I., and V. E. Zakharov (2005), Modulational instability of Stokes wave → Freak wave, *JETP Lett.*, *81*, 255–259.

Dysthe, K. B. (1979), Note on a modification to the nonlinear Schrödinger equation for application to deep water waves, *Proc. R. Soc. London, Ser. A*, *369*, 105–114.

Dysthe, K. B., H. E. Krogstad, and P. Müller (2008), Oceanic rogue waves, *Annu. Rev. Fluid Mech.*, *40*, 287–310.

Guenther, R. B., and J. W. Lee (1988), *Partial Differential Equations of Mathematical Physics and Integral Equations*, 536 pp., Prentice Hall, Englewood Cliffs, N. J.

Henderson, D., and H. Segur (2012), The Benjamin-Feir instability and propagation of swell across the Pacific, *Math. Comput. Simul.*, *82*, 1172–1184.

Henderson, D. M., M. S. Patterson, and H. Segur (2006), On the laboratory generation of two-dimensional, progressive, surface waves of nearly permanent form on deep water, *J. Fluid Mech.*, *559*, 413–427.

Henderson, D. M., H. Segur, and J. D. Carter (2010), Experimental evidence of stable wave patterns on deep water, *J. Fluid Mech.*, *658*, 247–278.

Huhnerfuss, H., P. A. Lange, and W. Walters (1985), Relaxation effects in monolayers and their contribution to water wave damping. II. The Marangoni phenomenon and gravity wave attenuation, *J. Colloid Interface Sci.*, *108*, 442–450.

Hunt, J. N. (1964), Dissipation in water waves, *Phys. Fluids*, *7*, 156.

Islas, A., and C. M. Schober (2011), Rogue waves and downshifting in the presence of damping, *Nat. Hazards Earth Syst. Sci.*, *11*, 383–399.

Janssen, P. A. E. M. (2003), Nonlinear four-wave interactions and freak waves, *J. Phys. Oceanogr.*, *33*, 863–884.

Janssen, P. A. E. M. (2004), *The Interaction of Ocean Waves and Wind*, 277 pp., Cambridge Univ. Press, Cambridge, U. K.

Komen, G. J., S. Hasselmann, and K. Hasselmann (1984), On the existence of a fully developed wind-sea spectrum, *J. Phys. Oceanogr.*, *14*, 1271–1285.

Lake, B. M., H. C. Yuen, H. Rungaldier, and W. E. Ferguson (1977), Nonlinear deep water waves, theory and experiment, part 2, *J. Fluid Mech.*, *83*, 49–74.

Lamb, H. (1932), Hydrodynamics, 6th ed., 730 pp., Dover, N. Y.

Lighthill, M. J. (1965), Contribution to the theory of waves in nonlinear dispersive systems, *J. Inst. Math. Appl.*, *1*, 296–306.

Lo, E., and C. C. Mei (1985), A numerical study of water-wave modulations based on a higher-order nonlinear Schrödinger equation, *J. Fluid Mech.*, *150*, 395–415.

Miles, J. W. (1967), Surface-wave damping in closed basins, *Proc. R. Soc. London, Ser. A*, *297*, 459–475.

Moskowitz, L. (1964), Estimates of the power spectrum for fully developed seas for wind speeds up to 20 to 40 knots, *J. Geophys. Res.*, *69*, 5161–5179.

Onorato, M., A. R. Osborne, and M. Serio (2006), Modulational instability in crossing sea states: A possible mechanism for the formation of freak waves, *Phys. Rev. Lett.*, *96*, 014503.

Ostrovsky, L. (1967), Propagation of wave packets and space-time self-focussing in a nonlinear medium, *Sov. J. Exp. Theor. Phys., 24*, 797–800.

Segur, H., D. Henderson, J. Carter, J. Hammack, C.-M. Li, D. Pheiff, and K. Socha (2005), Stabilizing the Benjamin-Feir instability, *J. Fluid Mech.*, *539*, 239–271.

Snodgrass, F. E., G. W. Groves, K. F. Hasselmann, G. R. Miller, W. H. Munk, and W. H. Powers (1966), Propagation of ocean swell across the Pacific, *Philos. Trans. R. Soc. London A*, *259*, 431–497.

Sulem, C., and P. L. Sulem (1999), *The Nonlinear Schrödinger Equation, Appl. Math. Sci. Ser.*, vol. *139*, 308 pp., Springer, New York.

Stokes, G. G. (1847), On the theory of oscillatory waves, *Trans. Camb. Phil. Soc*, *8*, 441.

Van Dorn, W. G. (1966), Boundary dissipation of oscillatory waves, *J Fluid Mech.*, *24*, 769–779.

Whitham, G. B. (1967), Nonlinear dispersion of water waves, *J. Fluid Mech.*, *27*, 399–412.

Zakharov, V. E. (1967), The wave stability in nonlinear media, *Sov. Phys. JETP*, *24*, 455–459.

Zakharov, V. E. (1968), Stability of periodic waves of finite amplitude on the surface of a deep fluid, *J. Appl. Mech. Tech. Phys.*, *9*, 190–194.